Jan 17, 2023

# Structure of human $Na_V1.6$ channel reveals $Na^+$ selectivity and pore blockade by 4,9-anhydro-tetrodotoxin

Yue Li[1,2,3]*, Tian Yuan[4]*, Bo Huang[6]*, Feng Zhou[6], Chao Peng[4], Xiaojing Li[1,3], Yunlong Qiu[1,3], Bei Yang[1], Yan Zhao[1,3]**, Zhuo Huang[4,5]**, Daohua Jiang[2,3]**

[1] National Laboratory of Biomacromolecules, CAS Center for Excellence in Biomacromolecules, Institute of Biophysics, Chinese Academy of Sciences, Beijing 100101, China

[2] Laboratory of Soft Matter Physics, Institute of Physics, Chinese Academy of Sciences, Beijing 100190, China

[3] University of Chinese Academy of Sciences, Beijing 100049, China

[4] State Key Laboratory of Natural and Biomimetic Drugs, Department of Molecular and Cellular Pharmacology, School of Pharmaceutical Sciences, Peking University Health Science Center, Beijing, 100191, China

[5] IDG/McGovern Institute for Brain Research, Peking University, Beijing, 100871, China;

[6] Beijing StoneWise Technology Co Ltd., 15 Haidian street, Haidian district, Beijing, China

* These authors contributed equally to this project.

** Correspondence emails: jiangdh@iphy.ac.cn (D.J.), huangz@hsc.pku.edu.cn (Z.H.) & zhaoy@ibp.ac.cn (Y.Z.)

## Abstract

The sodium channel $Na_V1.6$ is widely expressed in neurons of the central and peripheral nervous systems, which plays a critical role in regulating neuronal excitability. Dysfunction of $Na_V1.6$ has been linked to epileptic encephalopathy, intellectual disability and movement disorders. Here we present cryo-EM structures of human $Na_V1.6$/β1/β2 alone and complexed with a guanidinium neurotoxin 4,9-anhydro-tetrodotoxin (4,9-ah-TTX), revealing molecular mechanism of $Na_V1.6$ inhibition by the blocker. In the apo-form structure, two potential $Na^+$ binding sites were revealed in the selectivity filter, suggesting a possible mechanism for $Na^+$ selectivity and conductance. In the 4,9-ah-TTX-bound structure, 4,9-ah-TTX binds to a pocket similar to the tetrodotoxin (TTX) binding site, which occupies the $Na^+$ binding sites and completely blocks the channel. Molecular dynamics simulation results show that subtle conformational differences in the selectivity filter affect the affinity of TTX analogues. Taken together, our results provide important insights into $Na_V1.6$ structure, ion conductance, and inhibition.

# Introduction

Voltage-gated sodium ($Na_V$) channels mediate the generation and propagation of action potentials in excitable cells[1,2]. In humans, nine $Na_V$ channel subtypes ($Na_V1.1$-$1.9$) had been identified, which are involved in a broad range of physiological processes due to their tissue-specific distributions in various excitable tissues[3,4]. Subtype $Na_V1.6$, encoded by the gene *SCN8A*, is ubiquitously expressed in neurons of both the central nervous system (CNS) and the peripheral nervous system (PNS), especially enriched in the distal end of axon initial segment (AIS) and in the node of Ranvier of myelinated excitatory neurons. The $Na_V1.6$ channel is believed to play a primary role in the initiation and propagation of action potentials in those neurons by lowering the threshold voltage[5-11]. Emerging evidence suggests that $Na_V1.6$ is also expressed in some inhibitory interneurons and plays a role in establishing synaptic inhibition in the thalamic networks[12-14]. Compared with other $Na_V$ channel subtypes, $Na_V1.6$ possesses unique biophysical properties including activation at more hyperpolarized voltage, higher levels of persistent current and resurgent current, and higher frequency of repetitive neuronal firing in neurons such as cerebellar Purkinje cells[15-23]. These features make $Na_V1.6$ a critical and favorable mediator in regulating neuronal excitability in those neurons. Meanwhile, dozens of mutations in $Na_V1.6$ have been linked to human diseases, most of which exhibit gain-of-function phenotypes, increase neuronal excitability, and cause different types of epileptic encephalopathy[24-28]; whereas loss-of-function mutations are often associated with later onset seizures, intellectual disability, isolated cognitive impairment and movement disorders[29-31]. Thus, $Na_V1.6$ is an important drug target; effective and subtype-selective therapeutics are eagerly awaited for the treatment of $Na_V1.6$-related epilepsy and other neurological diseases.

Eukaryotic $Na_V$ channels are composed of a pore-forming α subunit and auxiliary β subunits[32]. The four-domain α subunit exerts voltage sensing, gate opening, ion

permeation, and inactivation[4,33]. Meanwhile, one or two β subunits bind to the α subunit to regulate $Na_V$ channel kinetics and trafficking. Among the four types of β subunits[34-37], β1 and β3 subunits non-covalently bind to the α subunit, while β2 and β4 subunits are covalently linked to the α subunit via a disulfide bond[32,38]. To date, high-resolution cryo-electron microscopy (cryo-EM) structures of seven mammalian $Na_V$ channels ($Na_V$1.1-1.5, $Na_V$1.7-1.8) have been reported[39-45]. Together with the resting-state[46], open-state[47] and multiple ligand-bound $Na_V$ channel structures[48-50], these structures revealed the general molecular mechanisms of voltage-sensing, electromechanically coupling, fast inactivation, sodium permeation, and ligand modulation. Among those $Na_V$ channel modulators, the guanidinium neurotoxin tetrodotoxin (TTX) has long been used as a useful tool to study $Na_V$ channels, which can potently inhibit $Na_V$1.1-1.4 and $Na_V$1.6-1.7 at nanomolar level (TTX-sensitive $Na_V$ channels), and less potently inhibit $Na_V$1.5, $Na_V$1.8, and $Na_V$1.9 at a micromolar concentration (TTX-insensitive $Na_V$ channels). The detailed binding mode of TTX had been revealed in the $Na_V$ channel-TTX complex structures[44,51]. Furthermore, two guanidinium neurotoxin derivatives, ST-2262 and ST-2530, were reported as potent and selective inhibitors for $Na_V$1.7, indicating that TTX analogs could potentially be developed as selective therapeutics[52,53]. Interestingly, 4,9-anhydro-tetrodotoxin (4,9-ah-TTX), a metabolite of TTX, has been reported to selectively block $Na_V$1.6 with a blocking efficacy of 40- to 160-fold higher than other TTX-sensitive $Na_V$ channels[54]. However, the structure of $Na_V$1.6 and how 4,9-ah-TTX blocks $Na_V$1.6 remain elusive.

In this study, we optimized a fully-functional shorter-form construct of human $Na_V$1.6 suitable for structural studies, and present cryo-EM structures of $Na_V$1.6/β1/β2 apo-form and in complex with 4,9-ah-TTX. Complemented with electrophysiological results and molecular dynamics (MD) simulations, our structures reveal $Na_V$1.6 structural features, sodium conductance, and pore-blockade by 4,9-ah-TTX.

# Results

## Construct optimization of $Na_V1.6$ for cryo-EM study

To conduct structural studies of $Na_V1.6$, human wide-type $Na_V1.6$ (named $Na_V1.6^{WT}$) was co-expressed with human β1 and β2 subunits in HEK293F cells and was purified similarly to previously reported $Na_V$ channels[41,44]. Although the amino acid sequence of $Na_V1.6$ is highly conserved with other $Na_V$ channel subtypes (*e.g.*, 70% identity with $Na_V1.7$); however, the purified $Na_V1.6^{WT}$ sample exhibited poor quality and did not permit high-resolution structural analysis (Supplementary Fig. 1a and b). Construct optimization had been proven to be successful in improving the sample quality of $Na_V1.7$ and $Na_V1.5$[55,56], we therefore carried out construct screening of human $Na_V1.6$ by removing unstructured intracellular loops and C-terminus. We found that deletion of S478-G692 between $D_I$ and $D_{II}$ ($Na_V1.6^{\Delta DI\text{-}DII}$), S1115-L1180 between $D_{II}$ and $D_{III}$ ($Na_V1.6^{\Delta DII\text{-}DIII}$), or R1932-C1980 of the C-terminus ($Na_V1.6^{\Delta Cter}$) showed improved sample homogeneity based on the size-exclusion chromatography (SEC) profiles (Supplementary Fig. 1a). Strikingly, when we combined these modifications and deleted all of the three unstructured regions, it displayed a sharp mono-disperse SEC profile, which is much better than that of $Na_V1.6^{WT}$ and any of the single-deletion constructs (Fig.1a and b, Supplementary Fig. 1a). We next examined the functional characteristics of the triple-deletion construct by whole-cell voltage-clamp recording of $Na_V1.6$-expressing HEK293T cells. The candidate construct exhibits typical voltage-dependent activation and inactivation (Fig. 1c). The resulting $V_{1/2}$ values of the voltage-dependence of activation and steady-state fast inactivation are −31.3 ± 0.3 mV (n=15) and −77.3 ± 0.2 mV (n=15), respectively, which are close to the reported $V_{1/2}$ values of human wide-type $Na_V1.6$ [57,58]. These results confirmed that the triple-deletion construct fulfills similar electrophysiological functions to the $Na_V1.6^{WT}$. The preliminary cryo-EM analysis of this triple-deletion construct showed that the micrograph contains a rich distribution of

monodisperse particles, which gave rise to much better 2D class averages with well-resolved features than the $Na_V1.6^{WT}$ (Supplementary Fig. 1b and c). Thus, this triple-deletion construct (named $Na_V1.6^{EM}$) was selected for further structural studies.

## The overall structure of human $Na_V1.6$

The purified $Na_V1.6^{EM}$/β1/β2 sample was frozen in vitreous ice for cryo-EM data collection (Supplementary Fig. 2). After processing, the final reconstruction map from the best class of ~41 k particles was refined to an overall resolution of 3.4 Å (Fig. 2a, Supplementary Fig. 3-5). As expected, the resulting $Na_V1.6^{EM}$/β1/β2 structure closely resembles the reported structures of human $Na_V$ channels due to the high sequence similarity (Fig. 2b). For example, the binding modes of the β subunits are consistent with the structures of human $Na_V1.7$/β1/β2 and $Na_V1.3$/β1/β2 [41,44]; the pore-forming α-subunit of $Na_V1.6^{EM}$ can be well superimposed with $Na_V1.7$ with a backbone (1107 residues) root mean square deviation (RMSD) of 1.4 Å (Fig. 2c). However, marked local conformational differences were observed between the two structures, especially in the extracellular loops (ECLs) (Fig. 2c and d). The ECLs are less conserved regions among the nine $Na_V$ channel subtypes (Supplementary Fig. 6a), which form the outer mouth of the selectivity filters (SFs) and contribute to the binding of β subunits. Superposition of the Domain I ECLs of $Na_V1.6^{EM}$ and $Na_V1.7$ shows that the $ECL_I$ of $Na_V1.6^{EM}$ lacks the short α2 helix which instead forms an extended hairpin-like turn (Fig. 2d). Importantly, the $ECL_I$ of $Na_V1.6^{EM}$ exhibits more N-linked glycosylation modification sites than $Na_V1.7$; N308-linked glycosylation site appears to be unique for $Na_V1.6$ based on the sequence alignment (Supplementary Fig. 6a). Although these structural differences in the ECLs do not affect the binding of β subunits to $Na_V1.6$ (Fig. 2a), the glycosylation and other modifications shape the surface properties of $Na_V1.6$, which play important roles in its trafficking, localization, and pathology[59,60]. For instance, a unique glycosylation site in the $ECL_I$ of $Na_V1.5$ blocks the binding of the β1 subunit to $Na_V1.5$[43].

We next compared the fast inactivation gate and intracellular activation gate between $Na_V1.6^{EM}$ and $Na_V1.7$, which only display subtle conformational shifts (Fig. 2e and f), indicating that those key structural elements are highly conserved to fulfill their similar biological roles. Consistently, the signature fast inactivation gate, Ile-Phe-Met motif (IFM-motif), binds tightly to its receptor site adjacent to the intracellular activation gate (Fig. 2e), resulting in a non-conductive activation gate constricted by A411, L977, I1464 and I1765 from the four S6 helices respectively (Fig. 2f). The van der Waals diameter of the activation gate is less than 6 Å, suggesting that the gate is functionally closed (Fig. 3a and b).

## Potential $Na^+$ sites in the SF

The ion path of $Na_V1.6$ has two constriction sites, the extracellular SF and intracellular activation gate respectively (Fig. 3a and b). The sodium selectivity of mammalian $Na_V$ channels is determined by the extracellular SF[61,62], which is composed of an Asp from $D_I$, Glu from $D_{II}$, Lys from $D_{III}$, and Ala from $D_{IV}$, known as the DEKA-locus[63,64]. Based on structural analysis, the acidic residues of the DEKA-locus are believed to act as a high-field strength site, which attracts and coordinates $Na^+$; and the Lys in $D_{III}$ was proposed as a favorable binding ligand for $Na^+$ which facilitates the ions passing through the SF[43,65]. In coincidence with other mammalian $Na_V$ channels[43,44], the SF of $Na_V1.6^{EM}$ adopts an asymmetric conformation composed of the DEKA-locus (Fig. 3b and c). No oblivious $Na^+$ binding site had been identified in previous structures of mammalian $Na_V$ channels. In contrast, densities for $Ca^{2+}$ were consistently reported in the structures of bacterial $Ca_VAb$ channel and mammalian $Ca_V1.1$, $Ca_V2.2$, and $Ca_V3.1$ channels[66-69]. Interestingly, two strong blobs of EM densities were observed in the SF of $Na_V1.6^{EM}$ (Fig. 3d and e), which are deduced as potential $Na^+$ binding sites because $Na^+$ ions are the only major cations in the solutions throughout the purification processes. The upper site (namely Na1) closely engages E936 of the DEKA-locus and an additional acidic residue E939 (Fig. 3c). The distances of this Na1 to the E936 and E939 are at

~3.5 Å, suggesting that $Na^+$ in Na1 site may still be hydrated. Meanwhile, D370 of the DEKA-locus contributes minorly to this $Na^+$ binding site at a distance of ~7.5 Å (Fig. 3c). This observation is in line with previous studies showing that E936/K1413 of the DEKA-locus are the most prominent residues for $Na^+$ permeation and selectivity, while D370 of the DEKA-locus is not absolutely required[63]. This potential Na1 site may represent the first step for $Na^+$ conductance, that is, E936 of the DEKA-locus attracts and captures one hydrated $Na^+$ from the extracellular solution with the assistance of E939. The second blob of density is located inside the SF, namely the Na2 site, which is about ~5.3 Å away from the Na1 site (Fig. 3d and e). Interestingly, the Na2 is close to the short side-chain residue A1705 of the DEKA-locus and is coordinated with the strictly conserved E373 at a distance of ~3.3 Å (Fig. 3c and d). We also noticed that D370/E936 of the DEKA-locus contribute negligibly to the Na2 at distances of 5.6-6.6 Å (Fig. 3c). Thus, we hypothesize that the Na2 may represent the second step for sodium conductance, that is, after captured and partially dehydrated in Na1 site, at least partially-dehydrated $Na^+$ can fit into the Na2 site which is going to enter the narrowest asymmetric constriction site of the SF. The possible partial dehydration of $Na^+$ in the Na2 site is reflected by its relatively weaker density compared to the Na1 (Fig. 3d and e). Furthermore, the K1413 points its long side-chain deep into the SF, forming the narrowest part of the SF. It has been proposed that this residue serves as a key coordination ligand in favor of $Na^+$ or $Li^+$ but is unfavorable for other cations[43]. In line with this hypothesis, $Na^+$ from the Na2 site can quickly pass through the SF and enter the central cavity accelerated by the amino group of the K1413. We found additional elongated density below the K1413 at a distance of ~3.5 Å, which may represent a third $Na^+$ site (namely Na3) (Fig. 3d and e). Consistently, previous MD simulations studies suggested that two $Na^+$ ions spontaneously occupy the symmetric SF of the bacterial $Na_V$ channels, and three $Na^+$ sites were proposed in the asymmetric SF of the eukaryotic $Na_V$ channel[70-72], which are similar to the Na2, Na3 sites and Na1-3 sites of our $Na_V1.6$ structure respectively.

In $Ca_V$ channels, the $Ca^{2+}$ binding sites were revealed in the SFs[66-68,73], suggesting a possible step-wise "knock-off" mechanism for $Ca^{2+}$ conducntance[66]. Superposition of the SFs of the $Na_V1.6^{EM}$ and the $Ca_VAb$ shows that the Na1 and Na2 sites are roughly at the same height levels as Ca1 and Ca2 sites in $Ca_VAb$, respectively (Fig. 3d and e). However, the two $Na^+$ sites are off the central axis of the SF, while the $Ca^{2+}$ sites are in the center (Supplementary Fig. 7). This difference is in agreement with the asymmetric characteristics of the SFs of mammalian $Na_V$ channels. As shown in the $Na_V1.6^{EM}$ structure, similar to the $Ca_V$ channels, two or more potential $Na^+$ sites exist in the SFs of $Na_V$ channels. In fact, the SFs of $Na_V$ and $Ca_V$ channels are closely related, point-mutations in the SF of the $Na_V$ channel can convert it into a highly $Ca^{2+}$ favorable channel[66,74]. Nevertheless, these subtle compositional and conformational differences at the SFs determine the ion selectivity and conductance.

## Blockade of $Na_V1.6$ by 4,9-ah-TTX

The guanidinium neurotoxin TTX and its derivatives can potently inhibit eukaryotic $Na_V$ channels[75]. TTX was reported to be more potent in inhibiting $Na_V1.6$ than other TTX-sensitive $Na_V$ channels[76]. Interestingly, one of the TTX metabolites, 4,9-ah-TTX, has been reported to preferentially block $Na_V1.6$ over the other eight $Na_V$ channel subtypes[54]. We first examined the TTX sensitivity of $Na_V1.6^{EM}$, $Na_V1.2$, and $Na_V1.7$, yielding $IC_{50}$ values of 1.9 nM (n=5), 4.9 nM (n=5), and 16.7 nM (n=4), respectively. Consistent with previous reports, TTX indeed favors $Na_V1.6$ (Supplementary Fig. 6c). Then we tested the inhibitory effects of 4,9-ah-TTX on $Na_V1.2$, $Na_V1.7$, and $Na_V1.6^{EM}$. As illustrated in Fig. 4a-c, 4,9-ah-TTX gradually inhibits both $Na_V1.7$ and $Na_V1.6^{EM}$ in a concentration-dependent manner. However, the resulting $IC_{50}$ values of 4,9-ah-TTX are significantly different, which are 257.9 nM (n=6) for $Na_V1.2$, 1340 nM (n=6) for $Na_V1.7$ and 52.0 nM (n=5) for $Na_V1.6^{EM}$, respectively (Fig. 4c). Those results confirmed that the potency of 4,9-ah-TTX is ~27-fold weaker than TTX in inhibiting $Na_V1.6^{EM}$, and 4,9-ah-TTX is indeed a $Na_V1.6$ preferred blocker.

To better understand the underlying mechanism of $Na_V1.6$ modulation by 4,9-ah-TTX, we solved the cryo-EM structure of $Na_V1.6^{EM}$/β1/β2 in complex with 4,9-ah-TTX (named $Na_V1.6^{4,9\text{-}ahTTX}$) at a resolution of 3.3 Å (Supplementary Fig. 4). The overall structure of $Na_V1.6^{4,9\text{-}ahTTX}$ is indistinguishable to the $Na_V1.6^{EM}$ (RMSD at 0.2 Å). However, unambiguous EM density located above the SF of $Na_V1.6^{4,9\text{-}ahTTX}$ was observed, which fits a 4,9-ah-TTX molecule very well (Fig. 4d and e, Supplementary Fig. 4b). A closer look shows that the 4,9-ah-TTX occupies the $Na^+$ binding sites and sticks into the SF of $Na_V1.6$ via extensive interactions (Fig. 4f). D370 and E373 from $D_I$, E936, and E939 from $D_{II}$, and D1708 from $D_{IV}$ form electrostatic interactions with the 4,9-ah-TTX, Y371 and K1413 also contribute to stabilizing the blocker by forming van der Waals interactions (Fig. 4f). Superposition of the $Na_V1.6^{4,9\text{-}ahTTX}$ and the TTX bound $Na_V1.7$ ($Na_V1.7^{TTX}$) show a very similar binding mode for the two blockers (Fig. 4f-h). This similar binding mode is reasonable because the chemical structures of TTX and 4,9-ah-TTX are very similar; secondly, these key interacting residues are identical among the TTX-sensitive $Na_V$ channels (Supplementary Fig. 6b). However, subtle conformational differences were observed. The 4,9-ah-TTX binds ~1.4 Å deeper in the pocket of $Na_V1.6$ than TTX in $Na_V1.7$ (Fig. 4h). In addition, the 4,9-ah-TTX lacks two hydroxyl groups at the 4 and 9 positions of TTX, which form two more hydrogen-bonds with E364 and G1407 of $Na_V1.7$, respectively (Fig. 4g). TTX should form the same interactions with $Na_V1.6$ as found in $Na_V1.7$. Thus, the binding of TTX to $Na_V1.6$ is stronger than the binding of 4,9-ah-TTX, which agrees with the higher potency of TTX in inhibiting $Na_V1.6$ than 4,9-ah-TTX (Fig. 4c and Supplementary Fig. 6c).

Then how does 4,9-ah-TTX preferentially inhibit $Na_V1.6$ over $Na_V1.7$ in a nearly identical pocket? By carefully checking the pore-loop sequences of $Na_V1.6$, we found that L1712 in the $D_{IV}$ P-loop of $Na_V1.6$ is a major different residue in the P-loop regions not similar to other $Na_V$ channels (Supplementary Fig. 6b). We tested the effect of 4,9-ah-TTX on L1712A mutant of $Na_V1.6$ ($Na_V1.6^{L1712A}$), the resulting $IC_{50}$ value of 4,9-ah-

TTX for $Na_V1.6^{L1712A}$ is 61.1 nM (n=4), which is close to that of the $Na_V1.6^{EM}$ (Supplementary Fig. 6d). This result suggests that L1712 is not relevant to the binding of 4,9-ah-TTX. To test whether the accessibility affects the binding of 4,9-ah-TTX, we substituted the $ECL_I$ of $Na_V1.6$ (F273-F356) with that of $Na_V1.7$ (F267-F347) or the $ECL_{III}$ (F1349-V1399) with that of $Na_V1.7$ (F1343-V1392), namely $Na_V1.6^{ECL1}$ and $Na_V1.6^{ECL3}$ respectively. Surprisingly, the substitution of the $ECL_I$ dramatically drops the $IC_{50}$ values of the 4,9-ah-TTX and TTX by 149-fold and 86-fold, respectively; in contrast, $ECL_{III}$ substitution only decreases the $IC_{50}$ values of the 4,9-ah-TTX and TTX by 2.6-fold and 1.1-fold respectively (Supplementary Fig. 6d and e). These results show that the ECL substitutions especially $ECL_I$ do affect the potency of TTX analogs, but do not discriminate them.

To further dissect the preferential inhibition of $Na_V1.6$ by 4,9-ah-TTX, we carried out MD simulations of TTX binding to $Na_V1.6$ or $Na_V1.7$, and 4,9-ah-TTX binding to $Na_V1.6$ or $Na_V1.7$. Six independent 100 ns MD simulations were performed for each complex and the trajectories were used for binding affinity calculations using the method of Molecular Mechanics with Generalized Born and Surface Area solvation (*MM/GBSA*)[77]. The simulation results show that the binding affinity of TTX to $Na_V1.6$ is significantly higher than that of 4,9-ah-TTX to $Na_V1.6$, and the affinity of 4,9-ah-TTX to $Na_V1.6$ is greater than 4,9-ah-TTX to $Na_V1.7$ (Supplementary Fig. 8a). These MD binding affinity results fairly agree with our electrophysiological results (Fig. 4c, Supplementary Fig. 6c). The simulations also show that there is only one predominant conformation for 4,9-ah-TTX binding to $Na_V1.6$; while there are four major conformations for 4,9-ah-TTX binding to $Na_V1.7$ (Fig. 5a, Supplementary Fig. 8b-f). More specifically, E373, E936, and E939 mainly contributed to the binding of 4,9-ah-TTX to $Na_V1.6$, consistent with our structural observation (Fig. 4f, Supplementary Fig. 8f); however, E930 and E927 of $Na_V1.7$, the counterparts of E939 and E936 in $Na_V1.6$, appeared to be very dynamic and contributed less stably to the binding of 4,9-ah-TTX (Fig. 5b). A contact analysis (Supplementary Fig.

9) was conducted to provide more details to understand the dynamics of the ligands (Supplementary Fig. 10). Specifically, E930 and E927 in $Na_V1.7$ interact with 4,9-ah-TTX with a frequency ranging from 21% to 87% for the most populated conformation cluster, whereas the frequency is over 90% for the interactions between such ligand and E939 and E936 in $Na_V1.6$. Superposition of the two representative conformations provides us an assumption that R922 of $P1_{II}$ helix is more flexible in $Na_V1.7$ than the equivalent R931 in $Na_V1.6$ because of the small side-chain T1409 on $P2_{III}$ helix, which in turn increases the flexibility of E930 and E927 and thereby negatively affects the binding of 4,9-ah-TTX to $Na_V1.7$ (Fig. 5c). To validate this assumption, we tested the potency of 4,9-ah-TTX on $Na_V1.6$ with double-mutations of M1416T/E1417I ($Na_V1.6^{M1416T/E1417I}$) using whole-cell voltage-clamp recordings. The resulting $IC_{50}$ value is 257 nM (n=5), which is 5-fold less potent than that of $Na_V1.6^{EM}$, in coincidence with the findings by MD simulations (Fig. 5d). Taken together, our results confirmed that TTX has the highest affinity to $Na_V1.6$ among the TTX-sensitive $Na_V$ channels; the TTX analog 4,9-ah-TTX is less potent than TTX in inhibiting $Na_V1.6$, but does exhibit preferential inhibition of $Na_V1.6$ over $Na_V1.7$.

## Pathogenic mutation map of $Na_V1.6$

The $Na_V1.6$ channels are abundantly distributed in neurons of both the CNS and the PNS. Compared to other Nav channel subtypes, the $Na_V1.6$ channel has unique properties including activation at more hyperpolarized potential and generating a large proportion of resurgent current and persistent current, which plays important roles in regulating neuronal excitability and repetitive firing[17,19]. To date, at least 16 gain-of-function mutations in $Na_V1.6$ causing hyperactivity are linked to Developmental and Epileptic Encephalopathy (DEE)[78]; meanwhile, 9 loss-of-function mutations in $Na_V1.6$ causing reduced neuronal excitability are associated with intellectual disability and movement disorders. We highlighted 14 gain-of-function and 7 loss-of-function mutations in our $Na_V1.6^{EM}$ structure (Fig. 6). The 14 gain-of-function mutations are mainly distributed in the VSDs, fast inactivation gate, and activation gate. In particular,

mutations G1475R, E1483K, M1492V, and A1650V/T target the fast inactivation gate, presumably causing overactivity of the $Na_V1.6$ variants by impairing the binding of the IFM-motif to its receptor site. Mutation N1768D, located at the end of the DIV-S6 helix, was reported to generate elevated persistent current and resurgent current[24,79], which may cause improper gate closing to generate these aberrant currents. Meanwhile, two loss-of-function variants, G964R and E1218K cause intellectual disability without seizure[30]. G964 is located in the middle of $S6_{II}$, which is believed to serve as a hinge in the pore-lining S6 helix during gating[80]. A G964R mutation can certainly impair the flexibility of the $S6_{II}$ helix; in addition, the additional long side-chain of the mutant can cause clashes with neighboring residues. E1218 belongs to the extracellular negatively-charged clusters (ENCs) of $VSD_{III}$, which play an important role in interacting with the positively-charged gating-charges. The E1218K mutation provides an opposite charge which can disrupt the voltage sensing. This mutant may also destabilize the variant, reflected by its significantly reduced express level[30].

## Discussion

In this study, we presented cryo-EM structures of human $Na_V1.6$/β1/β2 apo-form and complexed with the $Na_V1.6$ preferred blocker 4,9-ah-TTX. To facilitate the structural studies, we obtained the core construct of $Na_V1.6^{EM}$ which displayed improved sample quality. This construct and the structures can be a useful tool for future $Na_V1.6$-related structural and biochemical studies. The apo-form $Na_V1.6$ structure reveals three potential $Na^+$ sites, which are coordinated by the important residues in the SF, suggesting a possible mechanism for $Na^+$ recognition, selection, and conductance. By comparison with the $Ca^{2+}$ sites in bacterial and mammalian $Ca_V$ channels[66-69], the unique asymmetric SF of mammalian $Na_V$ channels provides a precise tunnel to separate $Na^+$ from other cations. However, the exact hydration state of those potential $Na^+$ sites cannot be identified here due to the resolution limit. Future high-resolution structure of $Na_V1.6$ would be required to investigate more detailed mechanisms of $Na^+$ conductance. The

4,9-anhydro-TTX bound $Na_V1.6$ structure demonstrated that 4,9-anhydro-TTX and its closely-related analog TTX share a similar binding pocket, which is composed of nearly identical residues above the SFs. However, TTX has greater potency than 4,9-anhydro-TTX in inhibiting $Na_V1.6$ very likely due to TTX can form two additional hydrogen bonds with $Na_V1.6$. Our MD simulations show that 4,9-anhydro-TTX exhibits a more stable binding mode and greater binding energy with $Na_V1.6$ than $Na_V1.7$. Specifically, the increased flexibility of E930 and E927 may cause the loose binding of 4,9-anhydro-TTX to $Na_V1.7$. Those results potentially explain the higher potency of TTX to $Na_V1.6$ than other TTX-sensitive $Na_V$ channels and the favorable inhibition of $Na_V1.6$ by 4,9-anhydro-TTX. In addition, an interesting observation needed to be mentioned here is the existence of some differences between the binding poses of 4,9-anhydro-TTX in the $Na_V1.6^{4,9\text{-ah-TTX}}$ EM structure and our MD simulation models (Fig. 4f, Supplementary Fig. 8f). The MD study was conducted with the assumption that the NH group of guanidine in 4,9-anhydro-TTX is fully protonated into $NH_2^+$. However, since such NH in the EM structure is only ~3 Å from the amine group of Y371, it implies an uncertainty of the protonation state of the guanidine of 4,9-anhydro-TTX. When we performed another MD study using unprotonated 4,9-anhydro-TTX and found that the ligand adopts a similar binding pose as observed in the EM structure. Our findings on the protonation state of 4,9-anhydro-TTX binding with $Na_V1.6$ requires further systemic investigation. Taken together, our results provide important insights into $Na_V$ channel structure, $Na^+$ selectivity, conductance, modulation by TTX, and its analog 4,9-anhydro-TTX.

# Methods

## Whole-cell recordings

HEK293T cells were maintained in Dulbecco's Modified Eagle Medium (DMEM, Gibco, USA) supplemented with 15% Fetal Bovine Serum (FBS, PAN-Biotech, Germany) at 37ºC and 5% $CO_2$. The P2 viruses of $Na_V1.6^{EM}$ and $Na_V1.6$ variants were obtained using Sf9 insect cells and used to infect HEK293T cells for 9 h. The plasmids expressing $Na_V1.2^{WT}$ or $Na_V1.7^{WT}$ were transfected into HEK293T cells using lipofectamine 2000 (Thermo Fisher Scientific, USA). 12-24 h after transfection or infection, whole-cell recordings were obtained using a HEKA EPC-10 patch-clamp amplifier (HEKA Electronic, Germany) and PatchMaster software (HEKA Electronic, Germany). The extracellular recording solution contained (in mM): 140 NaCl, 3 KCl, 1 $CaCl_2$, 1 $MgCl_2$, 10 Glucose, and 10 HEPES (310 mOsm/L, pH 7.30 with NaOH). The recording pipette intracellular solution contained (in mM): 140 CsF, 10 NaCl, 1 EGTA, and 10 HEPES (300 mOsm/L, pH 7.30 with CsOH). The pipettes were fabricated by a DMZ Universal Electrode puller (Zeitz Instruments, Germany) using borosilicate glass, with a resistance of 1.5-2.5 MΩ. The currents were acquired at a 50 kHz sample rate and series resistance ($R_s$) compensation was set to 70%~90%. All experiments were performed at room temperature.

Data analyses were performed using Origin 2020b (OriginLab, USA), Excel 2016 (Microsoft, USA), and GraphPad Prism 9.1.1 (GraphPad Software, USA). Steady-state fast inactivation (I-V) and conductance-voltage (G-V) relationships were fitted to Boltzmann equations:

$$I/I_{max}=1/(1+\exp((V_m-V_{1/2})/k))$$

$$G/G_{max}=1/(1+\exp((Vm-V_{1/2})/k))$$

$$G=I/(V_m-E_{Na})$$

where I is the peak current, G is conductance, $V_m$ is the stimulus potential, $V_{1/2}$ is the half-maximal activation potential, $E_{Na}$ is the equilibrium potential, and k is the slope factor.

To assess the potency of 4,9-anhydro-TTX and TTX on $Na_V$ channels, HEK293T cells were held at -120 mV and the inward sodium currents were elicited by a 50-ms step to -10 mV with a low frequency of 1/15 Hz. The concentration-response curves were fitted to a four-parameter Hill equation with constraints of Bottom=0 and Top=1:

$$Y=Bottom+(Top-Bottom)/(1+10^{(X-lgIC_{50})})$$

where Y is the value of $I_{Drug}/I_{Control}$, Top is the maximum response, Bottom is the minimum response, X is the lg of drug concentration, and $IC_{50}$ is the drug concentration producing the half-maximum response. The significance of fitted $IC_{50}$ values compared to the control was analyzed using the extra sum-of-squares F test.

## $Na_V1.6$-β1-β2 Cloning and Expression

The DNA fragments encoding human NaV1.6 (UniProt ID: Q9UQD0), β1 (Uniprot ID: Q07699), and β2 (Uniprot ID: O60939) were amplified from a HEK293 cDNA library. The full-length or truncated $Na_V1.6$, β1, and β2 genes were cloned into the pEG BacMam vector, respectively. For $Na_V1.6^{EM}$, residues of inter-domain linkers 478–692, 1115–1180, and 1932 to the last residue were deleted by PCR to optimize the biochemical properties of the purified protein sample. Specifically, NaV1.6EM was fused before a PreScission Protease recognition site, which is succeeded by a mCherry fluorescent protein and a Twin-Strep II tag at the C terminus. A superfolder green fluorescent protein (sfGFP) and His10 tag were introduced at the C terminus of β1. For protein expression, recombinant baculoviruses were generated in Sf9 cells using the Bac-to-Bac baculovirus expression system (Invitrogen, USA). HEK293F cells were cultured under 5% $CO_2$ at 37 °C and were used for transfection at a density of $2.5 \times 10^6$ cells/ml. The NaV1.6EM, β1, and β2 viruses were co-transfected into HEK 293F cells at a ratio of 1% (v/v)

supplemented with 1% (v/v) FBS. After 8-12h, sodium butyrate was added into the culture at a final concentration of 10 mM, and the cell was incubated for another 48 h under 30°C. Cells were then harvested by centrifugation at 1,640 x g for 5 minutes, and finally stored at −80°C after freezing in liquid nitrogen.

## Purification of human $Na_V1.6$-β1-β2 complex

The NaV1.6-β1-β2 complex was purified following a protocol as was applied in the purification of the NaV1.3-β1-β2 complex[41]. Cells expressing $Na_V1.6^{EM}$ complex were resuspended in buffer A (20 mM HEPES pH 7.5, 150 mM NaCl, 2 mM β-mercaptoethanol (β-ME), aprotinin (2 μg/mL), leupeptin (1.4 μg/mL), pepstatin A (0.5 μg/mL)) using a Dounce homogenizer and centrifuged at 100,000 × g for 1 h. After resuspension in buffer B (buffer A supplemented with 1% (w/v) n-Dodecyl-β-D-maltoside (DDM, Anatrace), 0.15% (w/v) cholesteryl hemisuccinate (CHS, Anatrace), 5 mM $MgCl_2$ and 5 mM ATP), the suspension was agitated at 4°C for 2 h and the insoluble fraction was removed by centrifugation again at 100,000 × g for 1 h. The supernatant containing solubilized $Na_V1.6^{EM}$ was then passed through Streptactin Beads (Smart-Lifesciences, China) via gravity flow at 4°C to enrich the protein complex. The resin was subsequently washed with buffer C (buffer A supplemented with 0.03% (w/v) glycol-diosgenin (GDN, Anatrace)) for 10 column volumes. The purified $Na_V1.6^{EM}$ complex was eluted with buffer D (buffer C plus 5 mM desthiobiotin (Sigma, USA)) and was subsequently concentrated to 1 mL using a 100 kDa cut-off Amicon ultra centrifugal filter (Merck Millipore, Germany). The concentrated protein sample was further purified by size exclusion chromatography (SEC) using a Superose 6 Increase 10/300 GL (GE Healthcare) column pre-equilibrated with the buffer E (20 mM HEPES pH 7.5, 150 mM NaCl, 2 mM β-ME, 0.007% GDN). Finally, the fractions containing homogeneous-distributed protein particles were collected and concentrated to ~4 mg/mL for cryo-EM sample preparation.

## Cryo-EM sample preparation and data acquisition

For the preparation of cryo-EM grids, 300-mesh Cu R1.2/1.3 grids (Quantifoil Micro Tools, Germany) were glow-discharged under H2-O2 condition for 60 s. A droplet of 2.5 μL of purified NaV1.6EM complex was applied to the grid followed by blotting for 4-5s at 4°C under 100% humidity using a Vitrobot Mark IV (Thermo Fisher Scientific, USA). In the case of the preparation of $Na_V1.6^{EM}$ complex with 4,9-anhydro-TTX, 50 μM 4,9-anhydro-TTX (Tocris, UK) was added to the sample before vitrification. Cryo-EM data were collected on a 300-kV Titan Krios transmission electron microscope (Thermo Fisher Scientific, USA) equipped with a Gatan K2 Summit Direct Electron Detector (Gatan, USA) located behind the GIF quantum energy filter (20 $e^-V$). SerialEM[81] was used to collect movie stacks at a magnification of ×130,000 (1.04 Å pixel size) with a nominal defocus range from –1.2 to –2.2 μm. A total dose of 50-60 e-/A2 was acquired for each movie stack under a dose rate of ~9.2 e-/($A^2$s) and dose-fractionated into 32 frames. A total of 3,985 and 2,929 movie stacks were collected for the apo- and 4,9-anhydro-TTX-bound NaV1.6 complex, respectively.

## Data Processing

For the data processing of apo and 4,9-anhydro-TTX-bound $Na_V1.6$ complex, a similar procedure was performed and a detailed diagram was presented in Supplementary Fig. 3 and 4. All the data were processed in RELION3.0[82] or cryoSPARC[83]. Movies were motion-corrected and dose-weighted using MotionCor2. Contrast transfer function (CTF) estimation was performed with GCTF[84]. Particles were picked using the AutoPick tool in RELION with templates and extracted into 256 × 256-pixel boxes. Several rounds of 2D and 3D classifications were performed to remove junk particles, followed by 3D autorefine, Bayesian polish, and CTF refinement to improve the map quality. The final EM density maps were generated by the non-uniform (NU) refinement in cryoSPARC and reported at 3.4 Å and 3.3 Å, respectively, according to the golden standard Fourier shell correlation (GSFSC) criterion.

## Model building

The sequence of human $Na_V1.6$ and $Na_V1.7$ were aligned using Jalview[85], and a homology model of $Na_V1.6$ was generated using the molecular replacement tool in PHENIX[86]. The atomic models of β1 and β2 subunits were extracted from the structure of $Na_V1.7$ (PDB ID: 6J8I). All of the models were fitted into the cryo-EM map as rigid bodies using the UCSF Chimera[87]. Restraints for 4,9-anhydro-TTX were derived by eLBOW in PHENIX and examined in *Coot*[88]. All residues were manually checked and adjusted to fit the map in *Coot* and were subsequently subjected to rounds of real-space refinement in PHENIX. Model validation was performed using the comprehensive validation (cryo-EM) in PHENIX. All figures were prepared with UCSF ChimeraX[89] or PyMOL (Schrödinger, USA)[90].

## Molecular dynamics simulations

The structures and force fields for protein, DMPC lipids, and ligands were prepared using the CHARMM-GUI website. The Amber ff14SB force field was used for both protein and lipids with the TIP3P model for water molecules[91]. The GAFF2 force field parameters were used for the ligands[92]. The simulated systems were solvated in water with 150 mM NaCl. The energy minimization was performed using the steepest descent method, followed by six equilibrium steps. During the 2 ns equilibrium steps, the protein backbone atoms were restrained to their initial positions using a harmonic potential with a force constant of 1 kcal $mol^{-1}$ $Å^{-2}$ and the restraints were subsequently removed. Berendsen's coupling scheme was used for both temperature and pressure[93]. Water molecules and all bond lengths to hydrogen atoms were constrained using LINCS[94]. Finally, six independent production runs were performed for 100 ns. The overall temperature of the system was kept constant, coupling independently for protein, lipids, and solvents at 303.15 K with a Nose-Hoover thermostat[95]. A constant pressure of 1 bar was maintained using a Parrinello–Rahman barostat in a semi-isotropic coupling type for x/y, and z directions respectively[96]. The temperature and pressure time constants of the

coupling were 1 and 5 ps, and the compressibility was $4.5 \times 10^{-5}$ $bar^{-1}$ for pressure. The integration of the equations of motion was performed by using a leapfrog algorithm with a time step of 2 fs. Periodic boundary conditions were implemented in all systems. A cutoff of 0.9 nm was implemented for the Lennard–Jones and the direct space part of the Ewald sum for Coulombic interactions. The Fourier space part of the Ewald splitting was computed by using the particle-mesh-Ewald method[97], with a grid length of 0.12 nm on the side and a cubic spline interpolation.

The binding affinities were calculated by MM/GBSA method[98-101]. The MM part consists of the bonded (bond, angle, and dihedral), electrostatic, and van der Waals interactions. The solvation free energies were obtained by using the generalized Born model (GB part), and the non-polar term is obtained from a linear relation to the solvent-accessible surface area (SA part). For each independent trajectory, the first 20 ns trajectory was discarded and 800 frames from 20-100 ns were used for MM/GBSA calculations. The final binding affinity for each ligand-protein complex was obtained by taking the average of the six independent trajectories. Regarding the clustering analysis, structure alignment was first performed for each two of the structures in the trajectory by using Least Squares algorithm which aligns two sets of structure by rotating and translating one of the structures so that the RMSD between matching atoms of the two structures is minimal. Then the clustering analysis was performed by using GROMOS[102] with a RMSD cut-off of 1.5 Å to determine the structurally similar clusters. All the simulations were performed using the GROMACS 2021 suite of programs[103].

## Data Availability

The UniProt accession codes for the sequences of human Nav1.6, β1 and β2 are Q9UQD0 [https://www.uniprot.org/uniprot/Q9UQD0], Q07699 [https://www.uniprot.org/uniprot/Q07699], and O60939 [https://www.uniprot.org/uniprot/O60939], respectively. The accession codes for the coordinates of Nav1.7, $Ca_VAb$, and $Ca_V3.1$ used in this study are 6J8J

518 [http://doi.org/10.2210/pdb6J8J/pdb], 4MS2 [http://doi.org/10.2210/pdb4MS2/pdb], and
519 6KZO [http://doi.org/10.2210/pdb6KZO/pdb], respectively. The three-dimensional cryo-
520 EM density maps of the human $Na_V1.6$/β1/β2 and $Na_V1.6$/β1/β2-4,9-anhydro-TTX have
521 been deposited in the EM Database under accession codes EMD-34387
522 [https://www.emdataresource.org/EMD-34387] and EMD-34388
523 [https://www.emdataresource.org/EMD-34388], respectively. The coordinates of the
524 $Na_V1.6$/β1/β2 and $Na_V1.6$/β1/β2-4,9-anhydro-TTX have been deposited in the Protein
525 Data Bank under accession codes 8GZ1 [http://doi.org/10.2210/pdb8GZ1/pdb] and
526 8GZ2 [http://doi.org/10.2210/pdb8GZ2/pdb], respectively.

## 527 Acknowledgments

528 We thank X. Huang, B. Zhu, X. Li, L. Chen, and other staff members at the Center for
529 Biological Imaging (CBI), Core Facilities for Protein Science at the Institute of
530 Biophysics, Chinese Academy of Science (IBP, CAS), and D. Sun at the SM10 Cryo-EM
531 Facility at the Institute of Physics, Chinese Academy of Sciences (IOP, CAS) for the
532 support in cryo-EM data collection. We thank Prof. Xuejun Cai Zhang for his helpful
533 discussions, and Yan Wu and Wei Fan for their research assistance service. This work is
534 funded by the Institute of Physics, Chinese Academy of Sciences (E0VK101 and
535 E2V4101 to D.J.), the National Natural Science Foundation of China (T2221001 and
536 32271272 to D.J., 92157102 to Y.Z., 31871083 and 82271498 to Z.H.), Chinese
537 Academy of Sciences Strategic Priority Research Program (Grant XDB37030304 to
538 Y.Z.), the National Natural Science Foundation of China (Grant 92157102 to Y.Z.), the
539 Chinese National Programs for Brain Science and Brain-like intelligence technology
540 (2021ZD0202102 to Z.H.).

## 541 Author Contributions

542 D.J., Z.H., and Y.Z. conceived and designed the experiments. Y.L. and X.L. prepared
543 samples for the cryo-EM study and made all the constructs. Y.Q. and B.Y. prepared cells
544 for protein expression. Y.L. collected cryo-EM data. Y.L. and D.J. processed the data,

and built and refined the models. Y.L. and T.Y. prepared figures. T.Y. collected the electrophysiology data. B.H., F.Z., and C.P. performed MD studies. Y.L., T.Y., B.H., Y.Z., Z.H., and D.J. analyzed and interpreted the results. L.Y. and D.J. wrote the paper, and all authors reviewed and revised the paper.

## Competing Interests

The Authors declare no competing interests.

## REFERENCES

1 Hodgkin, A. L. & Huxley, A. F. A quantitative description of membrane current and its application to conduction and excitation in nerve. *J Physiol* **117**, 500-544 (1952). https://doi.org:10.1113/jphysiol.1952.sp004764

2 Hille, B. Ionic channels in excitable membranes. 3rd Edn (OUP USA, 2001).

3 Yu, F. H. & Catterall, W. A. Overview of the voltage-gated sodium channel family. *Genome Biol* **4**, 207 (2003). https://doi.org:10.1186/gb-2003-4-3-207

4 Goldin, A. L. *et al.* Nomenclature of voltage-gated sodium channels. *Neuron* **28**, 365-368 (2000). https://doi.org:10.1016/s0896-6273(00)00116-1

5 Lorincz, A. & Nusser, Z. Molecular identity of dendritic voltage-gated sodium channels. *Science* **328**, 906-909 (2010). https://doi.org:10.1126/science.1187958

6 Li, T. *et al.* Action potential initiation in neocortical inhibitory interneurons. *PLoS Biol* **12**, e1001944 (2014). https://doi.org:10.1371/journal.pbio.1001944

7 Hu, W. *et al.* Distinct contributions of Na(v)1.6 and Na(v)1.2 in action potential initiation and backpropagation. *Nat Neurosci* **12**, 996-1002 (2009). https://doi.org:10.1038/nn.2359

8 Ye, M. *et al.* Differential roles of Na(V)1.2 and Na(V)1.6 in regulating neuronal excitability at febrile temperature and distinct contributions to febrile seizures. *Sci Rep* **8**, 753 (2018). https://doi.org:10.1038/s41598-017-17344-8

9 Boiko, T. *et al.* Compact myelin dictates the differential targeting of two sodium channel isoforms in the same axon. *Neuron* **30**, 91-104 (2001). https://doi.org:10.1016/s0896-6273(01)00265-3

10 Boiko, T. *et al.* Functional specialization of the axon initial segment by isoform-specific sodium channel targeting. *J Neurosci* **23**, 2306-2313 (2003). https://doi.org:10.1523/jneurosci.23-06-02306.2003

11 Van Wart, A. & Matthews, G. Expression of sodium channels Nav1.2 and Nav1.6 during postnatal development of the retina. *Neurosci Lett* **403**, 315-317 (2006). https://doi.org:10.1016/j.neulet.2006.05.019

12 Ogiwara, I. *et al.* Nav1.1 localizes to axons of parvalbumin-positive inhibitory interneurons: a circuit basis for epileptic seizures in mice carrying an Scn1a gene mutation. *J Neurosci* **27**, 5903-5914 (2007). https://doi.org:10.1523/jneurosci.5270-06.2007

13 Lorincz, A. & Nusser, Z. Cell-type-dependent molecular composition of the axon initial segment. *J Neurosci* **28**, 14329-14340 (2008). https://doi.org:10.1523/jneurosci.4833-08.2008

14 Makinson, C. D. *et al.* Regulation of Thalamic and Cortical Network Synchrony by Scn8a. *Neuron* **93**, 1165-1179.e1166 (2017). https://doi.org:10.1016/j.neuron.2017.01.031

15 Spampanato, J., Escayg, A., Meisler, M. H. & Goldin, A. L. Functional effects of two voltage-gated sodium channel mutations that cause generalized epilepsy with febrile seizures plus type 2. *J Neurosci* **21**, 7481-7490 (2001). https://doi.org:10.1523/jneurosci.21-19-07481.2001

16 Rush, A. M., Dib-Hajj, S. D. & Waxman, S. G. Electrophysiological properties of two axonal sodium channels, Nav1.2 and Nav1.6, expressed in mouse spinal sensory neurones. *J Physiol* **564**, 803-815 (2005). https://doi.org:10.1113/jphysiol.2005.083089

17 Smith, M. R., Smith, R. D., Plummer, N. W., Meisler, M. H. & Goldin, A. L. Functional analysis of the mouse Scn8a sodium channel. *J Neurosci* **18**, 6093-6102 (1998). https://doi.org:10.1523/jneurosci.18-16-06093.1998

18 Maurice, N., Tkatch, T., Meisler, M., Sprunger, L. K. & Surmeier, D. J. D1/D5 dopamine receptor activation differentially modulates rapidly inactivating and persistent sodium currents in prefrontal cortex pyramidal neurons. *J Neurosci* **21**, 2268-2277 (2001). https://doi.org:10.1523/jneurosci.21-07-02268.2001

19 Raman, I. M., Sprunger, L. K., Meisler, M. H. & Bean, B. P. Altered subthreshold sodium currents and disrupted firing patterns in Purkinje neurons of Scn8a mutant mice. *Neuron* **19**, 881-891 (1997). https://doi.org:10.1016/s0896-6273(00)80969-1

20 Jarecki, B. W., Piekarz, A. D., Jackson, J. O., 2nd & Cummins, T. R. Human voltage-gated sodium channel mutations that cause inherited neuronal and muscle channelopathies increase resurgent sodium currents. *J Clin Invest* **120**, 369-378 (2010). https://doi.org:10.1172/jci40801

21 Lewis, A. H. & Raman, I. M. Resurgent current of voltage-gated Na(+) channels. *J Physiol* **592**, 4825-4838 (2014). https://doi.org:10.1113/jphysiol.2014.277582

22 Raman, I. M. & Bean, B. P. Inactivation and recovery of sodium currents in cerebellar Purkinje neurons: evidence for two mechanisms. *Biophys J* **80**, 729-737 (2001). https://doi.org:10.1016/s0006-3495(01)76052-3

23 Khaliq, Z. M., Gouwens, N. W. & Raman, I. M. The contribution of resurgent sodium current to high-frequency firing in Purkinje neurons: an experimental and modeling study. *J Neurosci* **23**, 4899-4912 (2003). https://doi.org:10.1523/jneurosci.23-12-04899.2003

24 Veeramah, K. R. *et al.* De novo pathogenic SCN8A mutation identified by whole-genome sequencing of a family quartet affected by infantile epileptic encephalopathy and SUDEP. *Am J Hum Genet* **90**, 502-510 (2012). https://doi.org:10.1016/j.ajhg.2012.01.006

25 de Kovel, C. G. *et al.* Characterization of a de novo SCN8A mutation in a patient with epileptic encephalopathy. *Epilepsy Res* **108**, 1511-1518 (2014). https://doi.org:10.1016/j.eplepsyres.2014.08.020

26 Johannesen, K. M. *et al.* Genotype-phenotype correlations in SCN8A-related disorders reveal prognostic and therapeutic implications. *Brain* (2021). https://doi.org:10.1093/brain/awab321

27 Pan, Y. & Cummins, T. R. Distinct functional alterations in SCN8A epilepsy mutant channels. *J Physiol* **598**, 381-401 (2020). https://doi.org:10.1113/jp278952

28 Hargus, N. J., Nigam, A., Bertram, E. H., 3rd & Patel, M. K. Evidence for a role of Nav1.6 in facilitating increases in neuronal hyperexcitability during epileptogenesis. *J Neurophysiol* **110**, 1144-1157 (2013). https://doi.org:10.1152/jn.00383.2013

29 Blanchard, M. G. *et al.* De novo gain-of-function and loss-of-function mutations of SCN8A in patients with intellectual disabilities and epilepsy. *J Med Genet* **52**, 330-337 (2015). https://doi.org:10.1136/jmedgenet-2014-102813

30 Wagnon, J. L. *et al.* Loss-of-function variants of SCN8A in intellectual disability without seizures. *Neurol Genet* **3**, e170 (2017). https://doi.org:10.1212/nxg.0000000000000170

31 Liu, Y. *et al.* Neuronal mechanisms of mutations in SCN8A causing epilepsy or intellectual disability. *Brain* **142**, 376-390 (2019). https://doi.org:10.1093/brain/awy326

32 Isom, L. L., De Jongh, K. S. & Catterall, W. A. Auxiliary subunits of voltage-gated ion channels. *Neuron* **12**, 1183-1194 (1994). https://doi.org:10.1016/0896-6273(94)90436-7

33 Catterall, W. A., Goldin, A. L. & Waxman, S. G. International Union of Pharmacology. XLVII. Nomenclature and structure-function relationships of voltage-gated sodium channels. *Pharmacol Rev* **57**, 397-409 (2005). https://doi.org:10.1124/pr.57.4.4

34 Isom, L. L. *et al.* Primary structure and functional expression of the beta 1 subunit of the rat brain sodium channel. *Science* **256**, 839-842 (1992). https://doi.org:10.1126/science.1375395

35 Isom, L. L. *et al.* Structure and function of the beta 2 subunit of brain sodium channels, a transmembrane glycoprotein with a CAM motif. *Cell* **83**, 433-442 (1995). https://doi.org:10.1016/0092-8674(95)90121-3

36 Morgan, K. *et al.* beta 3: an additional auxiliary subunit of the voltage-sensitive sodium channel that modulates channel gating with distinct kinetics. *Proc Natl Acad Sci U S A* **97**, 2308-2313 (2000). https://doi.org:10.1073/pnas.030362197

37 Yu, F. H. *et al.* Sodium channel beta4, a new disulfide-linked auxiliary subunit with similarity to beta2. *J Neurosci* **23**, 7577-7585 (2003). https://doi.org:10.1523/jneurosci.23-20-07577.2003

38 O'Malley, H. A. & Isom, L. L. Sodium channel β subunits: emerging targets in channelopathies. *Annu Rev Physiol* **77**, 481-504 (2015). https://doi.org:10.1146/annurev-physiol-021014-071846

39 Pan, X. *et al.* Comparative structural analysis of human Na(v)1.1 and Na(v)1.5 reveals mutational hotspots for sodium channelopathies. *Proc Natl Acad Sci U S A* **118** (2021). https://doi.org:10.1073/pnas.2100066118

40 Pan, X. *et al.* Molecular basis for pore blockade of human Na(+) channel Na(v)1.2 by the μ-conotoxin KIIIA. *Science* **363**, 1309-1313 (2019). https://doi.org:10.1126/science.aaw2999

41 Li, X. *et al.* Structural basis for modulation of human Na(V)1.3 by clinical drug and selective antagonist. *Nat Commun* **13**, 1286 (2022). https://doi.org:10.1038/s41467-022-28808-5

42 Pan, X. *et al.* Structure of the human voltage-gated sodium channel Na(v)1.4 in complex with β1. *Science* **362** (2018). https://doi.org:10.1126/science.aau2486

43 Jiang, D. *et al.* Structure of the Cardiac Sodium Channel. *Cell* **180**, 122-134.e110 (2020). https://doi.org:10.1016/j.cell.2019.11.041

44 Shen, H., Liu, D., Wu, K., Lei, J. & Yan, N. Structures of human Na(v)1.7 channel in complex with auxiliary subunits and animal toxins. *Science* **363**, 1303-1308 (2019). https://doi.org:10.1126/science.aaw2493

45 Huang, X. *et al.* Structural basis for high-voltage activation and subtype-specific inhibition of human Na(v)1.8. *Proc Natl Acad Sci U S A* **119**, e2208211119 (2022). https://doi.org:10.1073/pnas.2208211119

46 Wisedchaisri, G. *et al.* Resting-State Structure and Gating Mechanism of a Voltage-Gated Sodium Channel. *Cell* **178**, 993-1003.e1012 (2019). https://doi.org:10.1016/j.cell.2019.06.031

47 Jiang, D. *et al.* Open-state structure and pore gating mechanism of the cardiac sodium channel. *Cell* **184**, 5151-5162.e5111 (2021). https://doi.org:10.1016/j.cell.2021.08.021

48 Clairfeuille, T. *et al.* Structural basis of α-scorpion toxin action on Nav channels. *Science* **363** (2019). https://doi.org:10.1126/science.aav8573

49 Ahuja, S. *et al.* Structural basis of Nav1.7 inhibition by an isoform-selective small-molecule antagonist. *Science* **350**, aac5464 (2015). https://doi.org:10.1126/science.aac5464

50 Jiang, D. *et al.* Structural basis for voltage-sensor trapping of the cardiac sodium channel by a deathstalker scorpion toxin. *Nat Commun* **12**, 128 (2021). https://doi.org:10.1038/s41467-020-20078-3

51 Shen, H. *et al.* Structural basis for the modulation of voltage-gated sodium channels by animal toxins. *Science* **362** (2018). https://doi.org:10.1126/science.aau2596

52 Pajouhesh, H. *et al.* Discovery of a selective, state-independent inhibitor of Na V 1.7 by modification of guanidinium toxins. *Sci Rep* **10**, 14791 (2020). https://doi.org:10.1038/s41598-020-71135-2

53 Beckley, J. T. *et al.* Antinociceptive properties of an isoform-selective inhibitor of Nav1.7 derived from saxitoxin in mouse models of pain. *Pain* **162**, 1250-1261 (2021). https://doi.org:10.1097/j.pain.0000000000002112

54 Rosker, C. *et al.* The TTX metabolite 4,9-anhydro-TTX is a highly specific blocker of the Na(v1.6) voltage-dependent sodium channel. *Am J Physiol Cell Physiol* **293**, C783-789 (2007). https://doi.org:10.1152/ajpcell.00070.2007

55 Jiang, D., Gamal El-Din, T., Zheng, N. & Catterall, W. A. Expression and purification of the cardiac sodium channel NaV1.5 for cryo-EM structure determination. *Methods Enzymol* **653**, 89-101 (2021). https://doi.org:10.1016/bs.mie.2021.01.030

56 Shen, H., Yan, N. & Pan, X. Structural determination of human $Na_v1.4$ and $Na_v1.7$ using single particle cryo-electron microscopy. *Methods Enzymol* **653**, 103-120 (2021). https://doi.org:10.1016/bs.mie.2021.03.010

57 Burbidge, S. A. *et al.* Molecular cloning distribution and functional analysis of the Nav1.6 Voltage-gated sodium channel from human brain. *Brain Res Mol Brain Res* **103**, 80-90 (2002). https://doi.org:10.1016/s0169-328x(02)00188-2

58 Zhao, J., O'Leary, M. E. & Chahine, M. Regulation of Nav1.6 and Nav1.8 peripheral nerve Na+ channels by auxiliary β-subunits. *J Neurophysiol* **106**, 608-619 (2011). https://doi.org:10.1152/jn.00107.2011

59 Jones, J. M. *et al.* Single amino acid deletion in transmembrane segment D4S6 of sodium channel Scn8a (Nav1.6) in a mouse mutant with a chronic movement disorder. *Neurobiol Dis* **89**, 36-45 (2016). https://doi.org:10.1016/j.nbd.2016.01.018

60 Solé, L. & Tamkun, M. M. Trafficking mechanisms underlying Nav channel subcellular localization in neurons. *Channels (Austin)* **14**, 1-17 (2020). https://doi.org:10.1080/19336950.2019.1700082

61 Hille, B. The permeability of the sodium channel to metal cations in myelinated nerve. *J Gen Physiol* **59**, 637-658 (1972). https://doi.org:10.1085/jgp.59.6.637

62 Hille, B. Ionic selectivity, saturation, and block in sodium channels. A four-barrier model. *J Gen Physiol* **66**, 535-560 (1975). https://doi.org:10.1085/jgp.66.5.535

63 Favre, I., Moczydlowski, E. & Schild, L. On the structural basis for ionic selectivity among $Na^+$, $K^+$, and $Ca^{2+}$ in the voltage-gated sodium channel. *Biophys J* **71**, 3110-3125 (1996). https://doi.org:10.1016/S0006-3495(96)79505-X

64 Sun, Y. M., Favre, I., Schild, L. & Moczydlowski, E. On the structural basis for size-selective permeation of organic cations through the voltage-gated sodium channel. Effect of alanine mutations at the DEKA locus on selectivity, inhibition by Ca2+ and H+, and molecular sieving. *J Gen Physiol* **110**, 693-715 (1997). https://doi.org:10.1085/jgp.110.6.693

65 Payandeh, J., Scheuer, T., Zheng, N. & Catterall, W. A. The crystal structure of a voltage-gated sodium channel. *Nature* **475**, 353-358 (2011). https://doi.org:10.1038/nature10238

66 Tang, L. *et al.* Structural basis for Ca2+ selectivity of a voltage-gated calcium channel. *Nature* **505**, 56-61 (2014). https://doi.org:10.1038/nature12775

67 Zhao, Y. *et al.* Cryo-EM structures of apo and antagonist-bound human $Ca_v3.1$. *Nature* **576**, 492-497 (2019). https://doi.org:10.1038/s41586-019-1801-3

68 Dong, Y. *et al.* Closed-state inactivation and pore-blocker modulation mechanisms of human $Ca_v2.2$. *Cell Rep* **37**, 109931 (2021). https://doi.org:10.1016/j.celrep.2021.109931

69 He, L. *et al.* Structure, gating, and pharmacology of human $Ca_v3.3$ channel. *Nat Commun* **13**, 2084 (2022). https://doi.org:10.1038/s41467-022-29728-0

70 Carnevale, V., Treptow, W. & Klein, M. L. Sodium Ion Binding Sites and Hydration in the Lumen of a Bacterial Ion Channel from Molecular Dynamics Simulations. *J Phys Chem Lett* **2**, 2504-2508 (2011). https://doi.org:10.1021/jz2011379

71 Guardiani, C., Rodger, P. M., Fedorenko, O. A., Roberts, S. K. & Khovanov, I. A. Sodium Binding Sites and Permeation Mechanism in the NaChBac Channel: A Molecular Dynamics Study. *J Chem Theory Comput* **13**, 1389-1400 (2017). https://doi.org:10.1021/acs.jctc.6b01035

72 Xia, M., Liu, H., Li, Y., Yan, N. & Gong, H. The mechanism of Na(+)/K(+) selectivity in mammalian voltage-gated sodium channels based on molecular dynamics simulation. *Biophys J* **104**, 2401-2409 (2013). https://doi.org:10.1016/j.bpj.2013.04.035

73 Wu, J. *et al.* Structure of the voltage-gated calcium channel Cav1.1 at 3.6 Å resolution. *Nature* **537**, 191-196 (2016). https://doi.org:10.1038/nature19321

74 Yue, L., Navarro, B., Ren, D., Ramos, A. & Clapham, D. E. The cation selectivity filter of the bacterial sodium channel, NaChBac. *J Gen Physiol* **120**, 845-853 (2002). https://doi.org:10.1085/jgp.20028699

75 Kao, C. Y. Tetrodotoxin, saxitoxin and their significance in the study of excitation phenomena. *Pharmacol Rev* **18**, 997-1049 (1966).

76 Tsukamoto, T. *et al.* Differential binding of tetrodotoxin and its derivatives to voltage-sensitive sodium channel subtypes ($Na_v1.1$ to $Na_v1.7$). *Br J Pharmacol* **174**, 3881-3892 (2017). https://doi.org:10.1111/bph.13985

77 Wang, E. *et al.* End-Point Binding Free Energy Calculation with MM/PBSA and MM/GBSA: Strategies and Applications in Drug Design. *Chem Rev* **119**, 9478-9508 (2019). https://doi.org:10.1021/acs.chemrev.9b00055

78 Gardella, E. *et al.* The phenotype of SCN8A developmental and epileptic encephalopathy. *Neurology* **91**, e1112-e1124 (2018). https://doi.org:10.1212/WNL.0000000000006199

79 Patel, R. R., Barbosa, C., Brustovetsky, T., Brustovetsky, N. & Cummins, T. R. Aberrant epilepsy-associated mutant Nav1.6 sodium channel activity can be targeted with cannabidiol. *Brain* **139**, 2164-2181 (2016). https://doi.org:10.1093/brain/aww129

80 Lenaeus, M. J. *et al.* Structures of closed and open states of a voltage-gated sodium channel. *Proc Natl Acad Sci U S A* **114**, E3051-E3060 (2017). https://doi.org:10.1073/pnas.1700761114

81 Mastronarde, D. N. Automated electron microscope tomography using robust prediction of specimen movements. *J Struct Biol* **152**, 36-51 (2005). https://doi.org:10.1016/j.jsb.2005.07.007

82 Zivanov, J. *et al.* New tools for automated high-resolution cryo-EM structure determination in RELION-3. *Elife* **7** (2018). https://doi.org:10.7554/eLife.42166

83 Punjani, A., Rubinstein, J. L., Fleet, D. J. & Brubaker, M. A. cryoSPARC: algorithms for rapid unsupervised cryo-EM structure determination. *Nat Methods* **14**, 290-296 (2017). https://doi.org:10.1038/nmeth.4169

84 Zhang, K. Gctf: Real-time CTF determination and correction. *J Struct Biol* **193**, 1-12 (2016). https://doi.org:10.1016/j.jsb.2015.11.003

85 Procter, J. B. *et al.* Alignment of Biological Sequences with Jalview. *Methods Mol Biol* **2231**, 203-224 (2021). https://doi.org:10.1007/978-1-0716-1036-7_13

86 Afonine, P. V. *et al.* Real-space refinement in PHENIX for cryo-EM and crystallography. *Acta Crystallogr D Struct Biol* **74**, 531-544 (2018). https://doi.org:10.1107/s2059798318006551

87 Pettersen, E. F. *et al.* UCSF Chimera--a visualization system for exploratory research and analysis. *J Comput Chem* **25**, 1605-1612 (2004). https://doi.org:10.1002/jcc.20084

88 Emsley, P., Lohkamp, B., Scott, W. G. & Cowtan, K. Features and development of Coot. *Acta Crystallogr D Biol Crystallogr* **66**, 486-501 (2010). https://doi.org:10.1107/s0907444910007493

89 Goddard, T. D. *et al.* UCSF ChimeraX: Meeting modern challenges in visualization and analysis. *Protein Sci* **27**, 14-25 (2018). https://doi.org:10.1002/pro.3235

90 DeLano, W. L. *The PyMOL Molecular Graphics System*, 2002).

91 Jo, S., Kim, T., Iyer, V. G. & Im, W. CHARMM-GUI: a web-based graphical user interface for CHARMM. *J Comput Chem* **29**, 1859-1865 (2008). https://doi.org:10.1002/jcc.20945

92 Wang, J., Wang, W., Kollman, P. A. & Case, D. A. Automatic atom type and bond type perception in molecular mechanical calculations. *J Mol Graph Model* **25**, 247-260 (2006). https://doi.org:10.1016/j.jmgm.2005.12.005

93 Berendsen, H. J. C., Postma, J. P. M., Vangunsteren, W. F., Dinola, A. & Haak, J. R. Molecular-Dynamics with Coupling to an External Bath. *J Chem Phys* **81**, 3684-3690 (1984). https://doi.org:Doi 10.1063/1.448118

94 Hess, B., Bekker, H., Berendsen, H. J. C. & Fraaije, J. G. E. M. LINCS: A linear constraint solver for molecular simulations. *Journal of Computational Chemistry* **18**, 1463-1472 (1997). https://doi.org:Doi 10.1002/(Sici)1096-987x(199709)18:12<1463::Aid-Jcc4>3.3.Co;2-L

95 Evans, D. J. & Holian, B. L. The Nose-Hoover Thermostat. *J Chem Phys* **83**, 4069-4074 (1985). https://doi.org:Doi 10.1063/1.449071

96 Parrinello, M. & Rahman, A. Polymorphic Transitions in Single-Crystals - a New Molecular-Dynamics Method. *J Appl Phys* **52**, 7182-7190 (1981). https://doi.org:Doi 10.1063/1.328693

97 Darden, T., York, D. & Pedersen, L. Particle Mesh Ewald - an N.Log(N) Method for Ewald Sums in Large Systems. *J Chem Phys* **98**, 10089-10092 (1993). https://doi.org:Doi 10.1063/1.464397

98 Srinivasan, J., Cheatham, T. E., Cieplak, P., Kollman, P. A. & Case, D. A. Continuum solvent studies of the stability of DNA, RNA, and phosphoramidate - DNA helices. *J Am Chem Soc* **120**, 9401-9409 (1998). https://doi.org:DOI 10.1021/ja981844+

99 Kollman, P. A. *et al.* Calculating structures and free energies of complex molecules: Combining molecular mechanics and continuum models. *Accounts Chem Res* **33**, 889-897 (2000). https://doi.org:10.1021/ar000033j

100 Genheden, S. & Ryde, U. The MM/PBSA and MM/GBSA methods to estimate ligand-binding affinities. *Expert Opin Drug Dis* **10**, 449-461 (2015). https://doi.org:10.1517/17460441.2015.1032936

101 Miller, B. R. *et al.* MMPBSA.py: An Efficient Program for End-State Free Energy Calculations. *J Chem Theory Comput* **8**, 3314-3321 (2012). https://doi.org:10.1021/ct300418h

817 102 Daura, X. *et al.* Peptide folding: When simulation meets experiment. *Angew Chem Int Edit* **38**, 236-240 (1999). https://doi.org:Doi 10.1002/(Sici)1521-3773(19990115)38:1/2<236::Aid-Anie236>3.3.Co;2-D

820 103 Van der Spoel, D. *et al.* GROMACS: Fast, flexible, and free. *Journal of Computational Chemistry* **26**, 1701-1718 (2005). https://doi.org:10.1002/jcc.20291

822

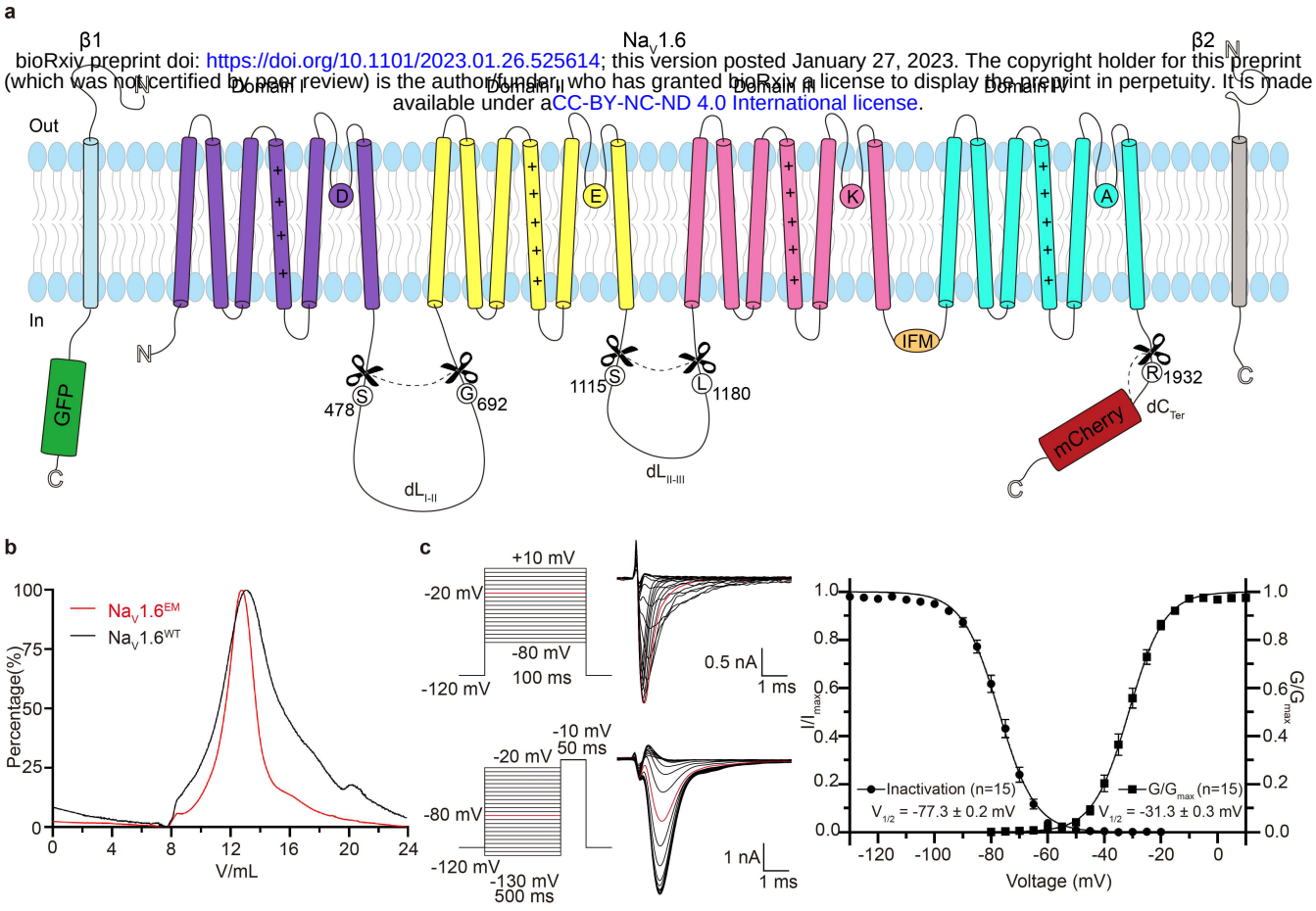


## Figure 1. Topology and functional characterization of the Na$_V$1.6$^{EM}$/β1/β2 complex.

**a**. Topology of the Na$_V$1.6/β1/β2 complex. The α subunit consists of DI (purple), DII (yellow), DIII (pink) and DIV (cyan) connected by intracellular linkers, a mCherry fluorescent protein tag fused at the C-terminus. Scissors indicate the truncated sites. The β1 fused with a GFP tag at the C-terminus and the β2 subunit are highlighted in light blue and gray respectively. The same color codes for Na$_V$1.6/β1/β2 are applied throughout the manuscript unless specified. **b**. Size exclusion chromatogram profiles of the purified Nav1.6$^{WT}$ (black) and the Nav1.6$^{EM}$ (red). **c**. Electrophysiological characterization of the Nav1.6$^{EM}$ construct. The voltage protocols and representative current traces are shown on the left panels. To characterize the voltage-dependence of activation, Na$_V$1.6$^{EM}$ expressing HEK293T cells were stimulated by a 100 ms test pulse varying from -80 mV to 10 mV in 5 mV increments from a holding potential of -120 mV, with a stimulus frequency of 0.2 Hz. To measure the steady-state fast inactivation, HEK293T cells were stimulated by a test step to -10 mV after a 500 ms prepulse varying from -130 mV to -20 mV in 5 mV increments, from a holding potential of -120 mV and a stimulus frequency of 0.2 Hz. The resulting normalized conductance-voltage (G/V) relationship (squares) and steady-state fast inactivation (circles) curves are shown on the right panel.

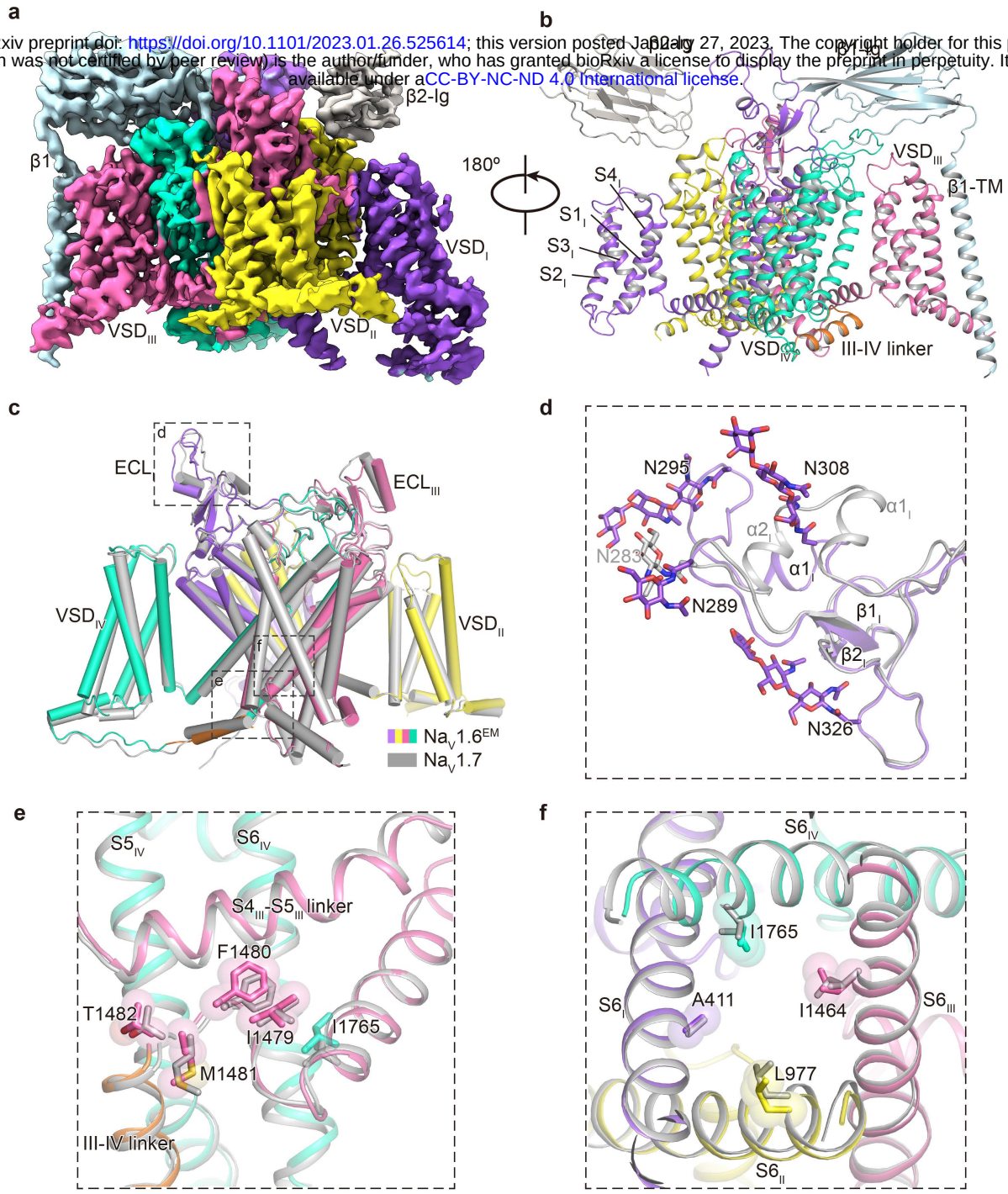


Figure 2. Cryo-EM structure of the $Na_V1.6^{EM}$/β1/β2 complex

**a-b**. The cryo-EM density map (**a**) and cartoon representation (**b**) of the $Na_V1.6^{EM}$/β1/β2 complex. **c**. Structural comparison of $Na_V1.6^{EM}$ and $Na_V1.7$ (PDB code: 7W9K, colored in gray). The black dashed-line squares indicate the areas shown in panels d, e, and f. **d**. Superimposition of the $ECL_I$ between $Na_V1.6^{EM}$ and $Na_V1.7$. N-linked glycosylation moieties are shown in sticks. **e**. Comparison of the IFM motif. The IFM motif were depicted side-chains in sticks and spheres with half transparency. **f**. Comparison of the intracellular activation gate of $Na_V1.6^{EM}$ and $Na_V1.7$ viewed from intracellular side. Key residues from four S6 helices were shown side-chains sticks and spheres with half transparency.

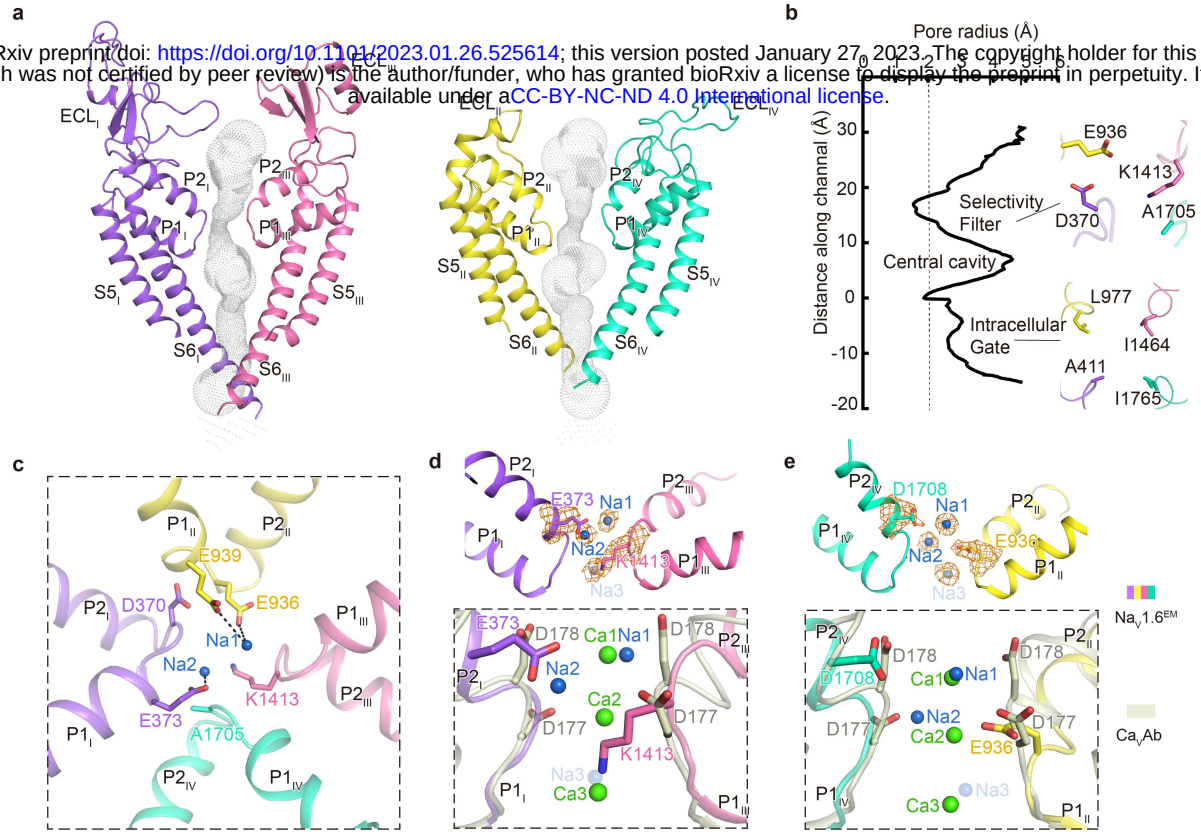


Figure 3. Potential $Na^+$ binding sites in the SF of $Na_V1.6^{EM}$

**a**. The ion conductance path of $Na_V1.6^{EM}$ calculated by HOLE. The diagonal repeats of pore domain only including the S5–S6 and pore-helices were shown for clarity. **b**. Plot of the pore radii of $Na_V1.6^{EM}$. The dashed line indicates pore radius at 2 Å. The key residues constituting the selectivity filter (SF) and the intracellular activation gate (AG) were shown as sticks. **c**. The SF of $Na_V1.6^{EM}$ viewed from the extracellular side. Potential $Na^+$ ions were shown as blue balls. Black dashed lines represent polar interactions. **d-e**. Comparison of the $Na^+$ binding sites of $Na_V1.6^{EM}$ and the $Ca^+$ binding sites of $Ca_VAb$ (PDB code: 4MS2, colored in gray). The diagonal repeats of DI and DIII (**d**), DII and DIV (**e**) are shown separately for clarity. The EM densities for putative $Na^+$ and key residues are shown in orange meshes contoured at 4 σ and 5 σ, respectively. A third possible $Na^+$ ion with weaker density contoured at 3 σ was shown as a light blue ball with half transparency. $Ca^+$ ions are shown as green balls.

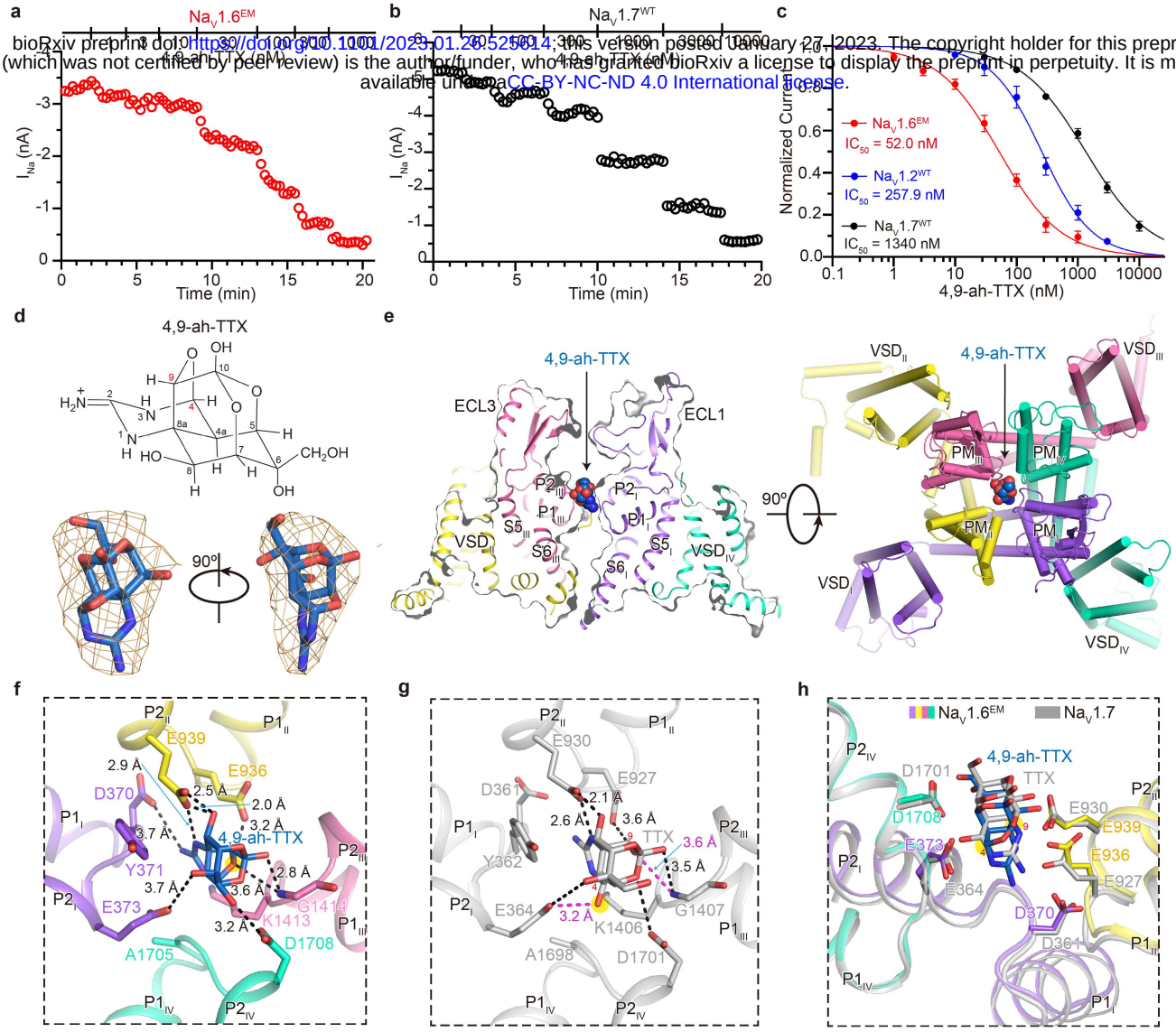


## Figure 4. Blockade of the Na$_V$1.6$^{EM}$ by 4,9-ah-TTX.

**a**-**b**. The peak currents of Na$_V$1.6$^{EM}$ (**a**) and Na$_V$1.7$^{WT}$ (**b**) in response to increasing concentrations of 4,9-ah-TTX. HEK293T cells were held at -120 mV and the inward sodium currents ($I_{Na}$) were elicited by a 50-ms step to -10 mV with a low frequency of 1/15 Hz. **c**. The concentration-response curves for the blockade of Na$_V$1.6$^{EM}$ (red), Na$_V$1.2$^{WT}$ (blue), and Na$_V$1.7$^{WT}$ (black) by 4,9-ah-TTX. **d**. The chemical structure of 4,9-ah-TTX (upper panel). The EM density for 4,9-ah-TTX shown in orange meshes contoured at 5 σ (lower panel). **e**. The 4,9-ah-TTX binding site in Na$_V$1.6$^{EM}$. Side (left panel) and top (right panel) view of Na$_V$1.6$^{EM}$ with 4,9-ah-TTX shown in spheres. **f**. Detailed interactions between 4,9-ah-TTX and Na$_V$1.6$^{EM}$. Key interacting residues of Na$_V$1.6$^{EM}$ were shown in sticks. Black dashed lines indicate electrostatic interactions between 4,9-ah-TTX and Na$_V$1.6$^{EM}$. **g**. Specific interactions between TTX and Na$_V$1.7 (PDB code: 6J8I, colored in gray). The additional hydrogen bonds between Na$_V$1.7 and the 4', 9' positions of TTX are highlighted in red. **h**. Structural comparison of Na$_V$1.6$^{4,9\text{-ahTTX}}$ and Na$_V$1.7$^{TTX}$. The side-chains of key residues in the Na$_V$1.6$^{EM}$ and Na$_V$1.7 depicted in sticks.

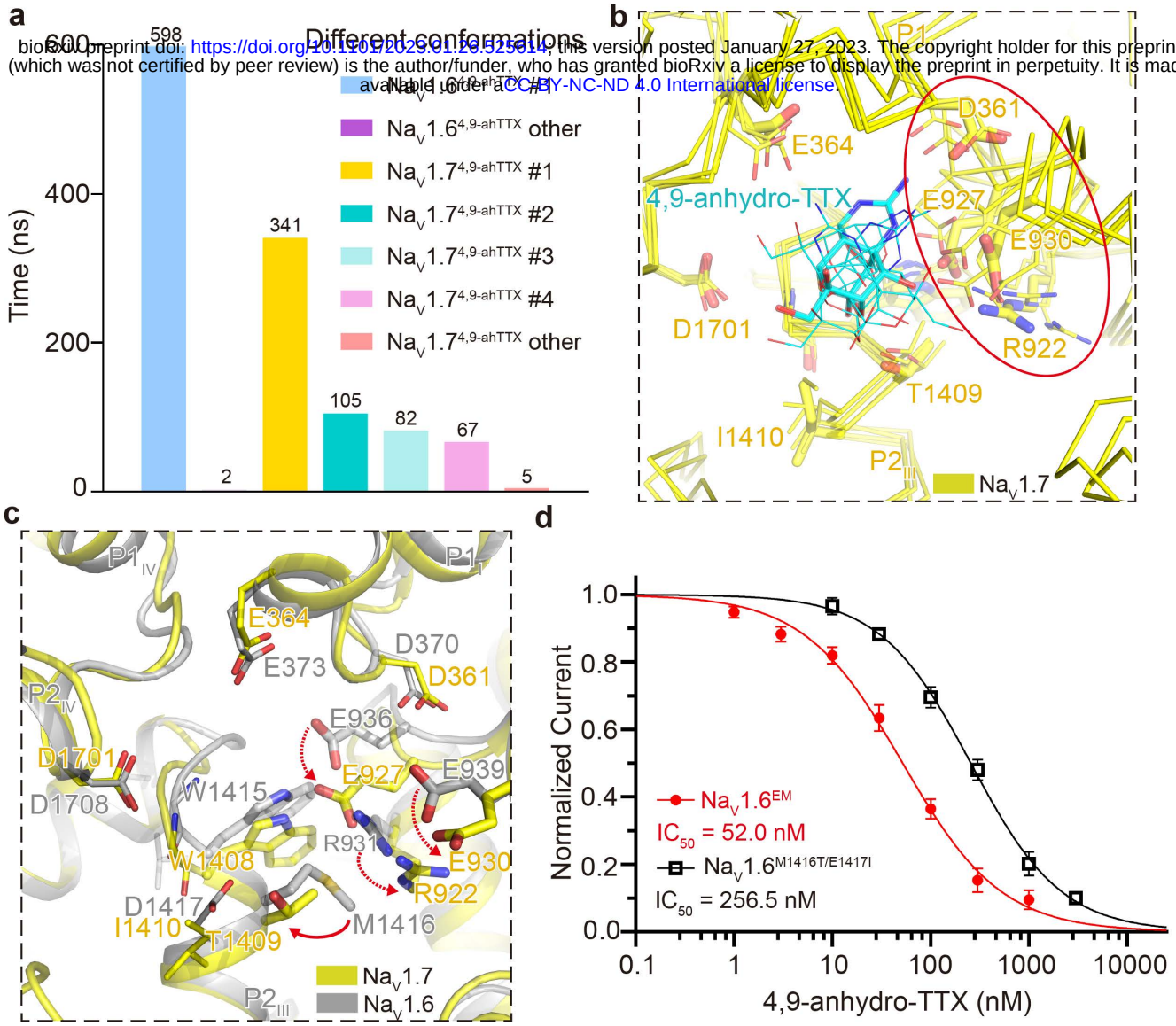


Figure 5. MD simulations of 4,9-ah-TTX binding to Na$_V$1.6 and Na$_V$1.7.

**a**. Cluster analysis of 600 ns molecular simulation trajectories for 4,9-ah-TTX binding with Na$_V$1.6 and Na$_V$1.7 respectively. The clustering was conducted by considering the ligand and protein residues within 5 Å of the ligand and using 1.5 Å as RMSD cutoff. **b**. Dynamic behaviors of 4,9-ah-TTX binding in Na$_V$1.7 pocket. Four major conformations of 4,9-ah-TTX bound Na$_V$1.7 were superimposed together, with the most dominant conformation displayed in yellow sticks and other three conformations in yellow lines. The highly flexible region including R922, E927, D361, E930 was indicated by a red circle. The 4,9-ah-TTX was colored in cyan, adopting different poses in the four major conformations. **c**. Illustration of the impact of the small side chain of T1409 to the flexibility of R922, E930, and E927. The red solid-line arrow indicates the size differences between T1409 of Na$_V$1.7 and M1416 of Na$_V$1.6. The gain of the extra flexibility for the side chains of R922, E930, and E927 was indicated by red dashed arrows. Conformation #1 of 4,9-ah-TTX bound Na$_V$1.6 was colored in gray and superimposed with conformation #2 of 4,9-ah-TTX bound Na$_V$1.7 which was colored in yellow. **d**. The concentration-response curves for the blockade of Na$_V$1.6$^{EM}$ and Na$_V$1.6$^{M1416T/E1417I}$ by 4,9-ah-TTX.

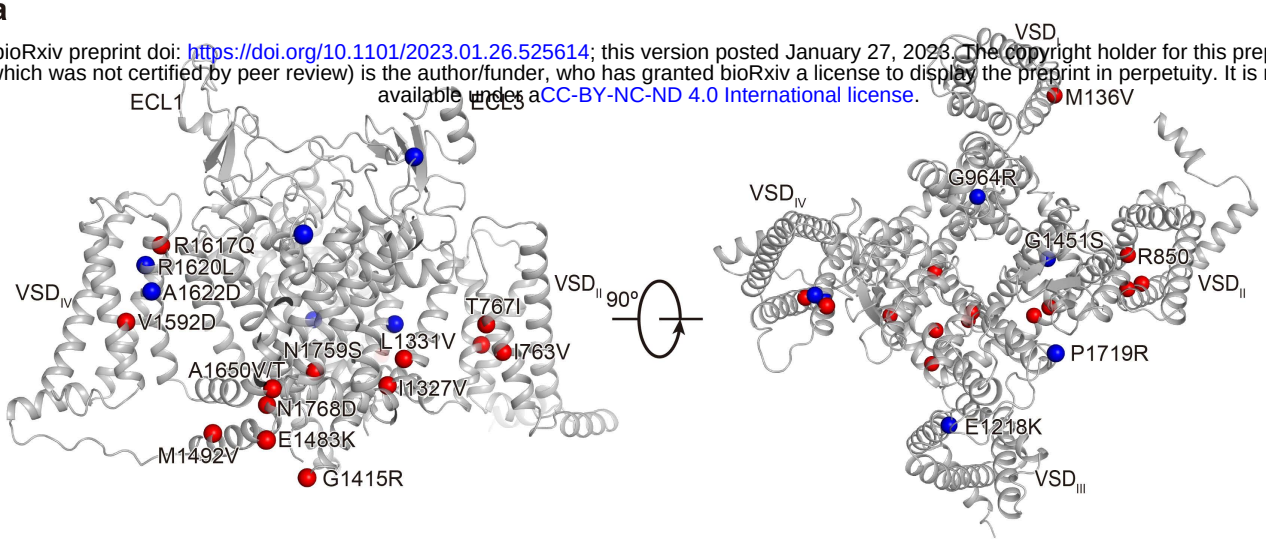


Figure 6. Mapping the pathogenic mutations on the $Na_V1.6^{EM}$.

**a**. Representative pathogenic mutations were mapped on the $Na_V1.6$ structure. Red and blue spheres represent the gain of function mutations (related to epilepsy) and loss of function mutations (related to intellectual disability), respectively.